Japanese Journal of Applied Physics 54, 08KE03 (2015) **REGULAR PAPER**
http://dx.doi.org/10.7567/JJAP.54.08KE03

Current–voltage and spectral-response characteristics of surface-activated-bonding-based InGaP/GaAs/Si hybrid triple-junction cells

Naoteru Shigekawa[1*], Jianbo Liang[1], Ryusuke Onitsuka[2], Takaaki Agui[2], Hiroyuki Juso[2], and Tatsuya Takamoto[2]

[1]*Graduate School of Engineering, Osaka City University, Osaka 558-8585, Japan*
[2]*Sharp Corporation, Yamatokoriyama, Nara 639-1186, Japan*
E-mail: shigekawa@elec.eng.osaka-cu.ac.jp

Received January 7, 2015; revised March 5, 2015; accepted May 9, 2015; published online July 10, 2015

We measured the current–voltage (*I*–*V*) and spectral-response characteristics of InGaP/GaAs/Si hybrid triple-junction cells that were fabricated by using surface-activated bonding methods. We found by spectral response measurements that the current generated in the Si-based bottom cell was lower than those in the top and middle cells under the conditions of an air mass of 1.5G and one sun. Furthermore we observed a discrepancy between the short-circuit current, which was obtained by subtracting the estimated contribution of Si ledges surrounding InGaP/GaAs mesas to the *I*–*V* characteristics, and the results of spectral response measurements. One possible model for explaining the discrepancy was discussed on the basis of the electrical coupling scheme between subcells. The intrinsic conversion efficiency of a 5 × 5 mm^2 triple-junction cell was crudely estimated to be ~26% by compensating for the shadow loss as well as subtracting the contribution of Si ledges.
© 2015 The Japan Society of Applied Physics

1. Introduction

Multijunction solar cells composed by stacking group-III–arsenide- or phosphide-based subcells with different bandgaps[1–7] have been promising candidates for next-generation solar cells[8] and have reportedly brought about the highest conversion efficiencies among a variety of solar cell structures.[9] Conversion efficiencies as high as >30% were reported for metal–organic vapor-phase epitaxy (MOVPE)-grown InGaP/InGaAs/Ge and InGaP/GaAs/InGaAs triple-junction cells.[6,7]

The main approach in research and development of multijunciton cells has been to increase the number of subcells while the current matching condition is fulfilled.[8] The concentrating photovoltaic (CPV) approach has been additionally employed.[10,11] Actually a conversion efficiency of 44.7% was reported for InGaP/GaAs/InGaAsP/InGaAs four-junction cells under the 297-times CPV condition.[12]

Another approach is to replace Ge-based or InGaAs-based bottom cells in the above structures with Si-based ones from the practical viewpoints. Group-III arsenides or phosphides/Si stacks are, consequently, likely to be the ideal structure for multijunction cells. The growth of compound-semiconductor-based cells on Si substrates or on Si-based bottom cells was reported.[13–15] It is still difficult, however, to grow III–V-on-Si multijunction cells because of (1) large differences in lattice constants and thermal expansion coefficients between compound semiconductors and Si[16] and (2) the frequent occurrence of anti-phase domains in the growth of group-III arsenide or phosphide layers on Si substrates.[17]

Multijunction cells can alternatively be fabricated by bonding subcells, or using the hybrid approach.[18–20] In the conventional bonding process, surfaces of samples must be carefully treated prior to the bonding and samples must be heated during their bonding in order to obtain excellent electrical characteristics of the bonding interfaces,[18,21] which are required for achieving high conversion efficiencies.

The surface-activated bonding (SAB), in which the samples are bonded to each other after their surfaces are activated by the Ar beam irradiation,[22–27] has enabled us to form semiconductor junctions without heating samples.[22] Consequently, junctions of dissimilar materials with different thermal expansion coefficients can be made by SAB. The structural properties of Si/Si junctions were previously examined.[23,24] The current–voltage (*I*–*V*) characteristics of SAB-based Si/Si, Si/GaAs, Si/InP, and Si/GaN junctions were reported.[25,26,28]

We investigated the electrical properties of SAB-based Si/GaAs junctions by measuring their *I*–*V* as well as capacitance–voltage characteristics.[29,30] We found by capacitance–voltage measurements that the band profiles of SAB-based GaAs/Si junctions revealed type-II features. We also measured the *I*–*V* characteristics of p–n junctions composed of semiconductor layers with different doping concentrations.[31] We found that the resistance across the bonding interface decreased as the concentrations of impurities in p- and n-doped layers increased. The lowest interface resistance that we obtained was 0.13 Ω·cm^2. Furthermore we fabricated InGaP/Si double-junction cells by SAB.[32] We measured their *I*–*V* characteristics and examined the relationship between the characteristics in the multijunction operation and those of the constituent subcells.

There were reports on SAB-based InGaP/GaAs/Si hybrid triple-junction cells, in which n-GaAs/n-Si isotype heterojunctions were employed for bonding. Conversion efficiencies of 20.5 (1 sun) and 23.6% (71 sun) were achieved.[33] We found by measuring the spectral responses of InGaP/GaAs/Si triple-junction cells that SAB-based GaAs/Si interfaces are transparent from the electrical and optical viewpoints and promising as a constituent of multijunction cells.[34] We also obtained results suggesting that the Si periphery of InGaP/GaAs mesas contributed to the measured characteristics of triple-junction cells. We recently reported on the *I*–*V* characteristics of a 5 × 5 mm^2 triple-junction cell.[35]

In this paper, by investigating the *I*–*V* characteristics of InGaP/GaAs/Si triple-junction cells in different configurations, we estimate the contribution of Si ledges surrounding the InGaP/GaAs mesas and subtract it from the cell characteristics. We find a discrepancy between the estimated actual short-circuit current of the triple-junction cells and currents generated in the respective subcells obtained by spectral-response measurements. A model for explaining the discrepancy based on the scheme of electrical coupling between subcells is discussed.

 © 2015 The Japan Society of Applied Physics

2. Experiments

2.1 Triple-junction cell fabrication and measurement method

An n-on-p Si-based bottom cell structure was prepared by the implantation of phosphor (P) ions to a high-resistive (10.9 Ω·cm) p-type Si(100) substrate and the subsequent rapid thermal annealing (900 °C and 1 min). The acceleration energy and dose in the implantation were 10 keV and 4.3×10^{14} cm^{-2}, respectively. The peak concentration of P atoms after the annealing was estimated to be 6×10^{19} cm^{-3} at a depth of 12 nm on the basis of a preparatory study by secondary ion mass spectroscopy. Boron (B) ions were also implanted on the back surface of the substrate so as to form contacts with a low resistance to the base. In addition, an n-on-p lattice-matched InGaP/GaAs double-junction cell structure was fabricated by growing a buffer layer, a top contact layer, an InGaP-based top cell structure, a tunnel-junction layer, a GaAs-based bottom cell structure, and a GaAs bonding layer on a GaAs substrate by MOVPE. The GaAs bonding layer was heavily p-type doped so as to achieve low contact resistances. Note that the respective layers were grown in the reverse order.

The double-junction cell structure was attached to the bottom cell structure by SAB without heating. The emitter thickness of the bottom cell structures was estimated to be ~10–20 nm because a preparatory study revealed that the bonding surfaces were etched by several nm owing to the Ar beam irradiation in the SAB process. After the GaAs substrate was selectively etched off, a conventional device process sequence, which consisted of InGaP/GaAs mesa etching, emitter contact formation, anti-reflection film deposition, Si mesa etching for bottom cell isolation (etching depth of ~1 µm), and base contact formation, was employed so that triple-junction cells with 1×1, 2×2, 4×4, and 5×5 mm^2 InGaP/GaAs mesa areas were fabricated. The geometry of devices defined that the effective portions in the mesas were 69.9, 79.6, 84.5, and 87.4% in the 1×1, 2×2, 4×4, and 5×5 mm^2 cells, which cause the shadow losses in the respective cells. InGaP/GaAs mesas in the respective cells are surrounded by Si ledges with an extension of 100 µm, which were essential for stably completing the bottom cell isolation process. A schematic cross section of a triple-junction cell is shown in Fig. 1. Details of the fabrication process were previously reported.[32,34]

The *I–V* characteristics of the respective cells were measured using a calibrated in-house solar simulator at room temperature. The solar irradiance under the conditions of an air mass of 1.5G and one sun was used. Dependencies of the short-circuit current I_{SC} on the solar irradiance were investigated between ~0.07 and one sun using mesh-shaped masks. Spectral-response measurements were also performed using Enlitech QE-R. LED modules were employed as bias light sources in measurements for multijunction cells.

2.2 Cell characterization

2.2.1 *I–V* characteristics under one-sun solar irradiance

The characteristics of the 5×5 mm^2 cell are shown in Fig. 2. I_{SC}, the open-circuit voltage V_{OC}, the fill factor, and the maximum output power are 2.845 mA, 2.875 V, 84.48%, and 6.908 mW, respectively, for the configuration in which the entire ledge was exposed to the incident solar irradiance. By approximately ignoring the contribution of the Si ledge, the short-circuit current density (J_{SC}) and conversion efficiency of this cell are found to be 11.38 mA/cm^2 and 27.63%, respectively. Such apparent J_{SC} and conversion efficiency of all cells, which were extracted from the measured characteristics using the same approximation, are shown in Fig. 3. We find that J_{SC} and the conversion efficiency increase as the InGaP/GaAs mesa size increases, which is attributed to the larger shadow losses in cells with the smaller mesa areas.

The *I–V* characteristics of the 5×5 mm^2 cell obtained in the configuration in which one-half of the Si ledge was masked are also shown in Fig. 2. I_{SC}, V_{OC}, the fill factor, and

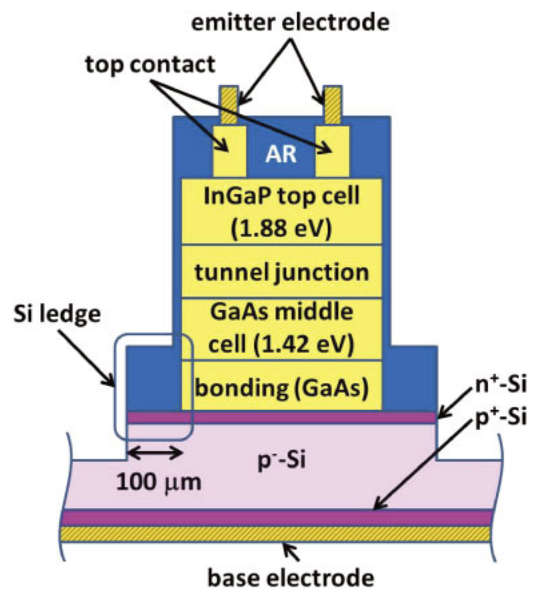

Fig. 1. (Color online) A schematic cross section of n-on-p InGaP/GaAs/Si triple-junction cells.

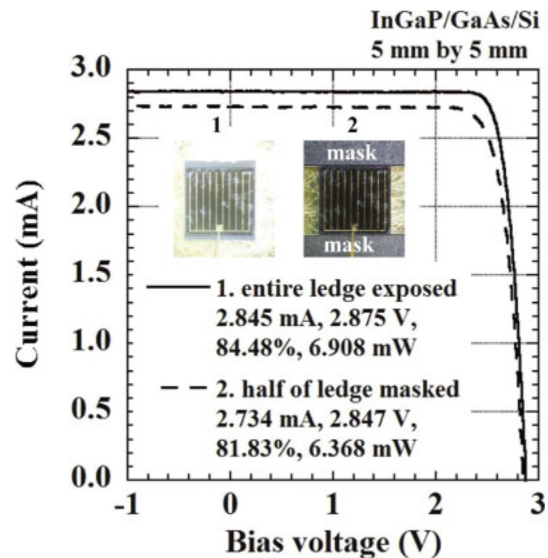

Fig. 2. (Color online) *I–V* characteristics of a 5×5 mm^2 InGaP/GaAs/Si triple-junction cell. Two curves for cells for the configuration in which the entire Si ledge was exposed (solid line) and one-half of the ledge was masked (dashed line) are shown. I_{SC}, V_{OC}, the fill factor, and the maximum output power extracted from the respective curves as well as photos for the respective configurations are also shown.

© 2015 The Japan Society of Applied Physics

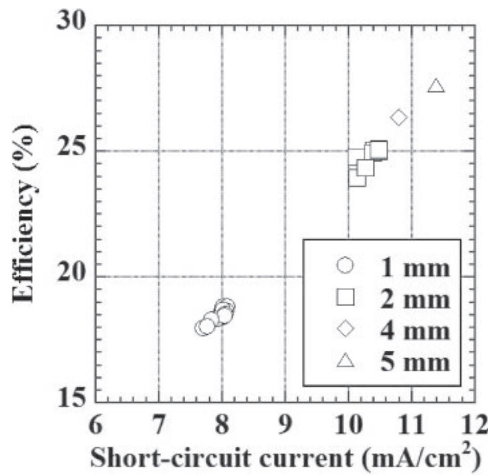

Fig. 3. The apparent J_{SC} and conversion efficiency of InGaP/GaAs/Si triple-junction cells with different mesa areas that are extracted from measurements with entire Si ledges exposed.

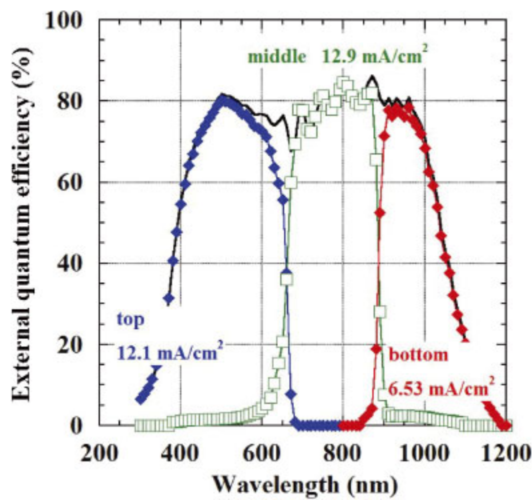

Fig. 4. (Color online) External quantum efficiency spectrum of a $5 \times 5\,mm^2$ triple-junction cell. Currents generated in the respective subcells are also shown.

the maximum output power in this configuration are 2.734 mA, 2.847 V, 81.83%, and 6.368 mW, respectively. Given that the observed differences in I_{SC} and the maximum output power between the two configurations were attributed to the contribution of one-half of Si ledge, I_{SC} and the maximum output power that should be obtained without the contribution of the Si ledge might be ≈2.62 mA and ≈5.83 mW, respectively. These values correspond to J_{SC} and a conversion efficiency of ~10 mA/cm^2 and ~23%, respectively. Furthermore by compensating for the shadow loss, the intrinsic conversion efficiency of this cell is estimated to be ~26%.

2.2.2 Spectral-response characteristics

The external quantum efficiency (EQE) spectrum of the $5 \times 5\,mm^2$ cell is shown in Fig. 4. Currents generated in the respective subcells under the conditions of an air mass of 1.5G and one sun, which were obtained using the EQE spectrum, are found to be 12.1, 12.9, and 6.53 mA/cm^2 for the top, middle, and bottom cells, respectively. Note that the actual J_{SC} (~10 mA/cm^2) is intermediate among currents generated in the respective subcells.

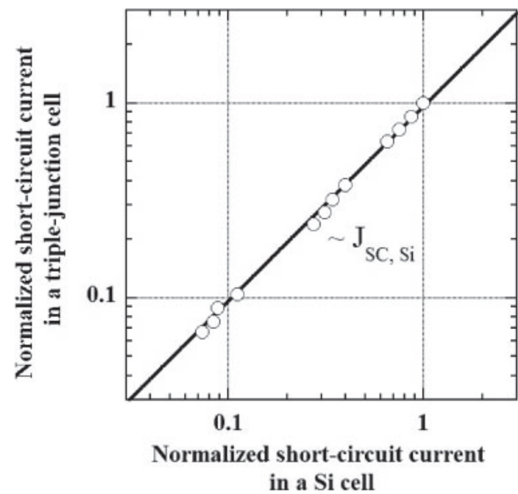

Fig. 5. Relationship between normalized J_{SC} of the $5 \times 5\,mm^2$ triple junction cell with one-half of Si ledge masked and that of a Si-based cell measured at various solar irradiances. A straight line indicating that J_{SC} values of the both cells are proportion to each other is also shown as guide to the eye.

2.2.3 Dependencies on magnitude of solar irradiance

The relationship between J_{SC} of the $5 \times 5\,mm^2$ triple-junction cells and that of Si cells obtained in measurements at various solar irradiances is shown in Fig. 5. J_{SC} of the triple-junction cell was measured in the configuration that one-half of Si ledge was masked. J_{SC} of each cell is normalized to J_{SC} for the one-sun irradiance. We found that J_{SC} in the triple-junction cell is almost proportional to that in the Si cell. We confirmed (data not shown) that J_{SC} in the triple-junction cell with the entire Si ledge exposed to the irradiance revealed the same behavior.

3. Discussion

The result that the actual J_{SC} of the triple-junction cells (~10 mA/cm^2) is intermediate among currents observed for the respective subcells in spectral response measurements is in disagreement with a simple view that the short-circuit current of multijunction cells should be limited by currents generated in subcells. One possible explanation for this disagreement is given by the optical coupling scheme.[36,37] Although the optical coupling reportedly plays a major role in multijunction cells under CPV conditions, the luminescent coupling factor under the one-sun irradiance is likely to be too small to explain the observed disagreement.[37]

Another mechanism that explains the result is explored for n-on-p double-junction cells with the short-circuit current of the top cell $J_{SC,1}$ larger than that of the bottom cell $J_{SC,2}$. The band diagram of such double-junction cells is schematically shown in Fig. 6 for the cells that are short-circuited. The difference in short-circuit current between subcells implies that the generation rate of carriers excited in the top cell should be higher than that of carriers excited in the bottom cell. A portion of the holes excited in the top cell is, consequently, assumed to condense in the p-doped layer in the tunnel junction. The condensation of holes plays a role in lowering the potential energy in this layer [(2) in Fig. 6].

 © 2015 The Japan Society of Applied Physics

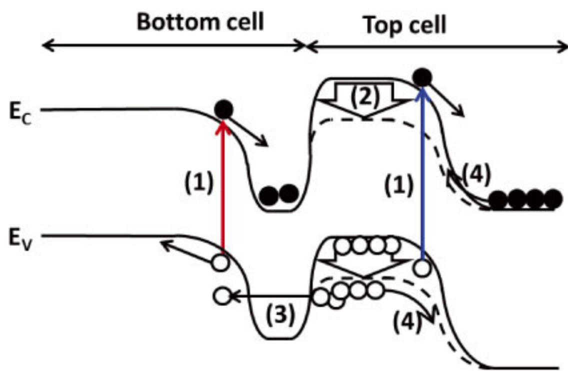

Fig. 6. (Color online) Conceptual band diagram of n-on-p double junction cells in which the solar irradiance excites carriers (1) so that the potential in the p+ layer of tunnel junctions is modulated owing to condensation of holes (2). Then holes are driven across the emitter of bottom cells (3). Simultaneously the minority carriers are electrically injected into the forward-biased top cell (4).

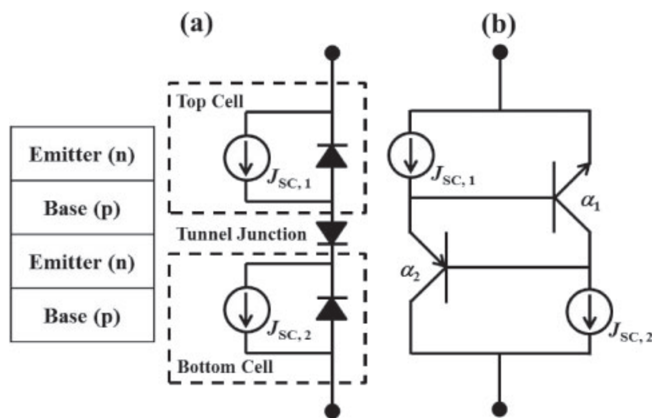

Fig. 7. An equivalent circuit of n-on-p double-junction cells composed of (a) three p–n diodes and (b) n–p–n and p–n–p bipolar transistors.

Such modulation in the potential is assumed to induce the injection of holes from the p-doped layer toward the base of the bottom cell across its 10–20-nm-thick emitter [(3) in Fig. 6] so that the current flowing through the bottom cell is larger than $J_{SC,2}$. In addition, the modulation in the potential should cause a forward bias to the top cell and enhance the injection of minority carriers in the top cell [(4) in Fig. 6]. Then the current occurring in the top cell is likely to be smaller than $J_{SC,1}$.

Figure 7(a) shows an equivalent circuit of double-junction cells discussed above. The circuit is composed of two current sources with magnitudes of $J_{SC,1}$ and $J_{SC,2}$ and three p–n diodes. Note that a p–n diode for the tunnel junction connecting the two subcells is explicitly displayed in this figure. Given that these p–n diodes are connected in a back-to-back configuration, they are equivalently replaced by n–p–n and p–n–p bipolar transistors, as is shown in Fig. 7(b). In this figure, α_1 and α_2 denote common-base current gains of the n–p–n and p–n–p bipolar transistors, respectively. The base and emitter currents in the n–p–n transistor are attributed to the holes generated in the top cell and electrons injected from the emitter of the top cell, respectively. The emitter current in the p–n–p transistor is due to the holes injected into the emitter of the bottom cell, which works as the base of this transistor. Using a similar scheme, the performances of heterojunction phototransistors were analyzed and the observed enhancements of optical gains were successfully explained.[38,39]

The short-circuit current of the double-junction cell $J_{SC,DJ}$ in this electrical coupling scheme is given by

$$J_{SC,DJ} = \frac{\alpha_1 \alpha_2 J_{SC,1} + J_{SC,2}}{1 + \alpha_1 \alpha_2 - \alpha_2}, \quad (1)$$

which should be intermediate between $J_{SC,1}$ and $J_{SC,2}$.

We note that both $J_{SC,1}$ and $J_{SC,2}$ are likely to be scaled as the solar irradiance. This means that $J_{SC,DJ}$ in Eq. (1) is likely to be scaled as the solar irradiance provided that α_1 and α_2 are independent of its magnitude. We also note that the performances of Si-based single-junction cells are free from photon recycling effects so that their J_{SC} is likely to be proportional to the irradiance. The result of measurements showing that J_{SC} of the triple-junction cell changes in proportion to that of Si cells, consequently, suggests that the features observed in J_{SC} of the triple-junction cell might be explained by the electrical coupling of subcells. The potentials of the base of the middle cells and the emitter of the bottom cells must be characterized for more quantitative discussions.

4. Conclusions

We successfully fabricated n-on-p InGaP/GaAs/Si hybrid triple-junction cells by the surface activated bonding of an MOVPE-grown lattice-matched InGaP/GaAs double-junction cell structure to an ion-implantation-based Si bottom cell structure. Their *I–V* characteristics were measured under the conditions of an air mass of 1.5G and one sun at room temperature. A J_{SC} of 11.38 mA/cm^2 and a conversion efficiency of 27.63% were achieved for a 5×5 mm^2 cell by approximately ignoring the contribution of the Si ledge with an extension of 100 μm. The actual J_{SC} of this cell was estimated to be ~10 mA/cm^2, which was in disagreement with results of spectral response measurements. One possible explanation on the basis of the electrical coupling between subcells was given. Furthermore the conversion efficiency of the cell was estimated to be ~26% by subtracting the contribution of the Si ledge and compensating for the shadow loss.

Acknowledgements

The authors are grateful to L. Chai, M. Morimoto, and S. Nishida for their assistance in device fabrication and characterization. This work was partly supported by the "Creative Research for Clean Energy Generation Using Solar Energy" project of the Core Research for Evolutional Science and Technology (CREST) program of Japan Science and Technology Agency (JST).

1) H. Sugiura, C. Amano, A. Yamamoto, and M. Yamaguchi, Jpn. J. Appl. Phys. **27**, 269 (1988).
2) J. M. Olson, S. R. Kurtz, A. E. Kibbler, and P. Faine, Appl. Phys. Lett. **56**, 623 (1990).
3) K. A. Bertness, S. R. Kurtz, D. J. Friedman, A. E. Kibbler, C. Kramer, and J. M. Olson, Appl. Phys. Lett. **65**, 989 (1994).
4) T. Takamoto, E. Ikeda, and H. Kurita, Appl. Phys. Lett. **70**, 381 (1997).
5) T. Takamoto, E. Ikeda, H. Kurita, M. Ohmori, M. Yamaguchi, and M.-J. Yang, Jpn. J. Appl. Phys. **36**, 6215 (1997).

© 2015 The Japan Society of Applied Physics

6) T. Takamoto, M. Kaneiwa, M. Imaizumi, and M. Yamaguchi, Prog. Photovoltaics **13**, 495 (2005).
7) J. F. Geisz, S. Kurtz, M. W. Wanlass, J. S. Ward, A. Duda, D. J. Friedman, J. M. Olson, W. E. McMahon, T. E. Moriarty, and J. T. Kiehl, Appl. Phys. Lett. **91**, 023502 (2007).
8) M. A. Green, Prog. Photovoltaics **9**, 123 (2001).
9) Web [http://www.nrel.gov/ncpv/images/efficiency_chart.jpg].
10) M. Yamaguchi and A. Luque, IEEE Trans. Electron Devices **46**, 2139 (1999).
11) K. Nishioka, T. Takamoto, T. Agui, M. Kaneiwa, Y. Uraoka, and T. Fuyuki, Sol. Energy Mater. Sol. Cells **90**, 1308 (2006).
12) F. Dimroth, M. Grave, P. Beutel, U. Fiedeler, C. Karcher, T. N. D. Tibbits, E. Oliva, G. Siefer, M. Schachtner, A. Wekkeli, A. W. Bett, R. Krause, M. Piccin, N. Blanc, C. Drazek, E. Guiot, B. Ghyselen, T. Salvetat, A. Tauzin, T. Signamarcheix, A. Dobrich, T. Hannappel, and K. Schwarzburg, Prog. Photovoltaics **22**, 277 (2014).
13) T. Soga, K. Baskar, T. Kato, T. Jimbo, and M. Umeno, J. Cryst. Growth **174**, 579 (1997).
14) M. R. Lueck, C. L. Andre, A. J. Pitera, M. L. Lee, E. A. Fitzgerald, and S. A. Ringel, IEEE Electron Device Lett. **27**, 142 (2006).
15) M. J. Archer, D. C. Law, S. Mesropian, M. Haddad, C. M. Fetzer, A. C. Ackerman, C. Ladous, R. R. King, and H. A. Atwater, Appl. Phys. Lett. **92**, 103503 (2008).
16) O. Moutanabbir and U. Gösele, Annu. Rev. Mater. Res. **40**, 469 (2010).
17) Ph. Komninou, J. Stoemenos, G. P. Dimitrakopulos, and Th. Karakostas, J. Appl. Phys. **75**, 143 (1994).
18) K. Tanabe, A. F. i. Morral, H. A. Atwater, D. J. Aiken, and M. W. Wanlass, Appl. Phys. Lett. **89**, 102106 (2006).
19) K. Tanabe, K. Watanabe, and Y. Arakawa, Sci. Rep. **2**, 349 (2012).
20) H. Mizuno, K. Makita, and K. Matsubara, Appl. Phys. Lett. **101**, 191111 (2012).
21) M. J. Jackson, B. L. Jackson, and M. S. Goorsky, J. Appl. Phys. **110**, 104903 (2011).
22) H. Takagi, K. Kikuchi, R. Maeda, T. R. Chung, and T. Suga, Appl. Phys. Lett. **68**, 2222 (1996).
23) H. Takagi, R. Maeda, T. R. Chung, N. Hosoda, and T. Suga, Jpn. J. Appl. Phys. **37**, 4197 (1998).
24) H. Takagi, R. Maeda, N. Hosoda, and T. Suga, Jpn. J. Appl. Phys. **38**, 1589 (1999).
25) M. M. R. Howlader, T. Watanabe, and T. Suga, J. Vac. Sci. Technol. B **19**, 2114 (2001).
26) M. M. R. Howlader, T. Watanabe, and T. Suga, J. Appl. Phys. **91**, 3062 (2002).
27) C. Wang, E. Higurashi, and T. Suga, Jpn. J. Appl. Phys. **47**, 2526 (2008).
28) N. Shigekawa, N. Watanabe, and E. Higurashi, Proc. 3rd Int. IEEE Workshop Low-Temperature Bonding for 3D Integration, 2012, p. 109.
29) J. Liang, T. Miyazaki, M. Morimoto, S. Nishida, N. Watanabe, and N. Shigekawa, Appl. Phys. Express **6**, 021801 (2013).
30) N. Shigekawa, J. Liang, M. Morimoto, and S. Nishida, ECS Trans. **64** [5], 235 (2014).
31) J. Liang, S. Nishida, M. Morimoto, and N. Shigekawa, Electron. Lett. **49**, 830 (2013).
32) N. Shigekawa, M. Morimoto, S. Nishida, and J. Liang, Jpn. J. Appl. Phys. **53**, 04ER05 (2014).
33) K. Derendorf, S. Essig, E. Oliva, V. Klinger, T. Roesener, S. P. Philipps, J. Benick, M. Hermle, M. Schachtner, G. Siefer, W. Jäger, and F. Dimroth, IEEE J. Photovoltaics **3**, 1423 (2013).
34) N. Shigekawa, L. Chai, M. Morimoto, J. Liang, R. Onitsuka, T. Agui, H. Juso, and T. Takamoto, Proc. 40th IEEE Photovoltaic Specialists Conf., 2014, p. 534.
35) N. Shigekawa, L. Chai, M. Morimoto, J. Liang, R. Onitsuka, T. Agui, H. Juso, and T. Takamoto, presented at 6th World Conf. Photovoltaic Energy Conversion (WCPEC-6), 2014, 5WeO.4.6.
36) M. A. Steiner, J. F. Geisz, I. García, D. J. Friedman, A. Duda, W. J. Olavarria, M. Young, D. Kuciauskas, and S. R. Kurtz, IEEE J. Photovoltaics **3**, 1437 (2013).
37) D. Derkacs, D. T. Bilir, and V. A. Sabnis, IEEE J. Photovoltaics **3**, 520 (2013).
38) R. A. Milano, T. H. Windhorn, E. R. Anderson, G. E. Stillman, R. D. Dupuis, and P. D. Dapkus, Appl. Phys. Lett. **34**, 562 (1979).
39) N. Chand, P. A. Houston, and P. N. Robson, IEEE Trans. Electron Devices **32**, 622 (1985).

© 2015 The Japan Society of Applied Physics